# Lattice Vibrations in Trigonal HgS

R. ZALLEN AND G. LUCOVSKY
*Xerox Research Laboratories, Rochester, New York 14603*

AND

W. TAYLOR,* A. PINCZUK, AND E. BURSTEIN

*University of Pennsylvania,† Philadelphia, Pennsylvania 19104*

(Received 22 December 1969)

Trigonal HgS (cinnabar) possesses a twofold-coordinated low-symmetry structure highly unusual among $A^nB^{8-n}$ crystals. The cinnabar structure is based on close-packed helical chains, with six atoms per unit cell and $D_3$ symmetry. We have investigated the long-wavelength optical phonons in HgS via their interaction with light: reflectivity in the far infrared and Raman scattering in the visible. Classical-oscillator analysis of the complex reststrahlen spectra has been carried out to obtain frequencies, infrared strengths, dielectric dispersion properties, and, in addition, polariton dispersion curves for the $A_2$ and $E$ modes. The Raman scattering is dominated by the $A_1$ lines, and the relative magnitude of the TO and LO $E$ lines indicate that the atomic-displacement contribution to the polarizability modulation exceeds the electro-optic. Marked complementarity between Raman and infrared intensities is noted and connected to a view of the HgS lattice as a geometric perturbation on the rocksalt structure. The frequencies (given as $\tilde{\nu}$ in $cm^{-1}$) of the observed lattice fundamentals and their symmetry assignments are: 29(39), $A_2$; 45, $A_1$; 87(91), $E$; 108(147), $E$; 110(141), $A_2$; 256, $A_1$; 280(288), $E$; 333(357), $A_2$; and 342(350), $E$. (Frequencies in parentheses refer to the longitudinal representatives of the infrared-active modes.) A simple model and the observed frequencies are used to derive approximate vibrational eigenvectors for the symmetric $A_1$ modes, and, on the basis of electrostatic (TO-LO) and anisotropy ($A_2$-$E$) splittings as well as Raman and infrared intensities, the three eigenvectors corresponding to 108–110 $cm^{-1}$ are taken to consist largely of rigid-sublattice motions analogous to the optical modes in simple diatomic crystals such as NaCl. The effective charge of these latter vibrations is estimated as $e^*/e=0.4$.

## 1. INTRODUCTION

AMONG the simplest and best understood solids are the insulating crystals formed by $AB$ binary compounds with eight valence electrons per atom pair. This large class includes the alkali halides, the alkaline-earth salts, the III-V and II-VI semiconductors isoelectronic to the diamond-structure elemental crystals, and the noble-metal halides. Almost all of these crystals possess structures, at low pressure and temperature, belonging to one or the other of two types: the "ionic" octahedrally and cubically coordinated NaCl and CsCl structures, and the "covalent" tetrahedrally coordinated zinc-blende and wurtzite structures. (An inventory of 80 such crystals reveals but five exceptions.[1]) The chalcogenides of mercury are unique in that, in addition to displaying a zinc-blende modification, they crystallize in a dihedrally coordinated low-symmetry structure, the cinnabar structure. HgS possesses this structure under normal conditions while HgSe and HgTe, zinc blende at atmospheric pressure, transform to cinnabar structure at modest pressures.

In this paper we describe an experimental investigation of the lattice vibrations of trigonal cinnabar-structure HgS. The long-wavelength optical phonons have been studied by means of their interaction with light: reflectivity in the far infrared and Raman scattering of visible light (HgS is a semiconductor with a band gap of 2 eV).[2] A discussion of the cinnabar structure is given in Sec. 2, and a group-theoretical analysis of the zone-center phonons is presented in Sec. 3. Experimental aspects are discussed in Sec. 4, and the observed spectra are displayed in Sec. 5. A classical-oscillator analysis of the complex reststrahlen spectra is carried out to obtain frequencies, infrared strengths, and dielectric dispersion properties in Sec. 6, and polariton dispersion curves in Sec. 7. An inventory of the observed lattice fundamentals is given in Sec. 8, and implications of the Raman intensities are discussed in Sec. 9. In Sec. 10 we derive information about the vibrational eigenvectors from our experimental results in conjunction with some simple models. Effective charges are discussed in Sec. 11, and our principal findings are summarized in Sec. 12.

## 2. CINNABAR STRUCTURE

As we are concerned with the vibrations of atoms about their equilibrium positions, we must first consider the crystal lattice itself. The unit cell, containing three HgS molecules, is shown in Fig. 1. The structure

* Present address: Natural Philosophy Department, University of Edinburgh, Scotland.

† Supported in part by the U. S. Army Research Office (Durham) and the Advanced Research Projects Agency.

[1] R. W. G. Wyckoff, *Crystal Structures* (Wiley, New York, 1963), Vol. 1. The five are HgS, HgO, BN, AuI, and InBi. AuI and InBi possess complex structures. BN, isoelectronic to C, possesses a layer structure akin to graphite. HgO, in addition to a cinnabar form, displays an orthorhombic modification, also dihedrally coordinated. Several other materials, such as SiC and ZnS, exhibit stacking polytypes which are intermediate between zinc blende and wurtzite.

[2] R. Zallen, in *II-VI Semiconducting Compounds*, edited by D. G. Thomas (Benjamin, New York, 1967), p. 877.

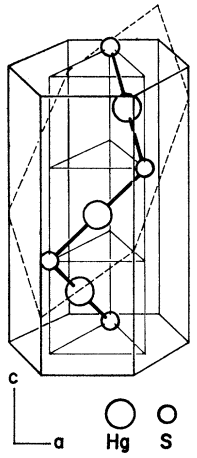


FIG. 1. Unit cell of trigonal HgS. The structure has been slightly idealized; S-Hg-S is not quite a straight angle as depicted (cf. Fig. 9).

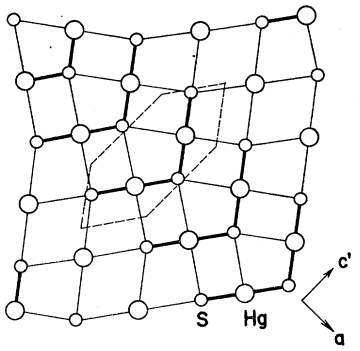


FIG. 2. Projection on an $a$-$c'$ plane, where $a$ denotes [1000] and $c'$ denotes [01$\bar{1}\bar{1}$] in the hexagonal indexing. The atomic positions are approximately coplanar.

consists of -S-Hg-S-Hg-S- helical chains, six atoms to a turn.[3] Nearest-neighbor (NN) bonds make roughly a right-angle turn at the sulfurs (105°), with close to a straight-angle continuation at the mercurys (172°). The chains are arranged in close packing, so that the space lattice is hexagonal. The shortest interchain bond length is 30% greater than the NN bond length of 2.36 Å. The weak bonding between chains is reflected in the cleavage behavior; the crystal cleaves only in planes containing the $c$ axis (no broken chains). The dihedral intrachain bond in trigonal HgS is significantly stronger than the tetrahedral bond (2.53 Å) occurring in the cubic modification.

The twofold coordination is indicative of covalent bonding, with each Hg and S contributing two valence electrons to their NN bonds, and the remaining four electrons at each sulfur presumably forming two lone-pair orbitals. Concordant with this is the fact that the Hg-S-Hg angle is close to the S-S-S bond angle in sulfur.[1] This bonding is quite different from that in tetrahedrally coordinated zinc blende and wurtzite, in which every valence electron participates and there are no lone pairs.

Bonding between chains is at least partly ionic; each atom has four next-nearest neighbors (NNN) on neighboring chains, all of opposite polarity. If we include both nearest and next-nearest neighbors, each atom might be regarded as sixfold coordinated, surrounded by six atoms (2 NN+4 NNN) of the opposite species. In this sense, HgS may be viewed as possessing a distorted rocksalt structure, the six neighbors of each site defining a distorted octahedral configuration. This aspect of the structure is depicted in Fig. 2, which presents atomic projections on a plane which corresponds to a (100) plane in the equivalent rocksalt setting. The relation between Figs. 1 and 2 is indicated by the dashed hexagon which is the intersection of the plane of Fig. 2 with the hexagonal prism, enclosing a single chain, of Fig. 1.

This correspondence[4] between the rocksalt and cinnabar structures, which we will find relevant to the most strongly infrared-active modes (and to other results discussed in Secs. 9–11), is revealed in another way. Of the nine binary compounds which Zn, Cd, and Hg form with S, Se, and Te, all but HgS possess zinc-blende–wurtzite structures at zero pressure and temperature. (HgS displays its zinc-blende phase above 600°K.[5]) At high pressure, the Zn and Cd salts transform to the NaCl structure, while HgSe and HgTe transform to the cinnabar structure.[6] Thus the cinnabar structure is the densely packed modification for the Hg compounds, playing the same role for HgS, HgSe, and HgTe as does the NaCl structure for the Zn and Cd chalcogenides. (The preference of Hg for a dihedral rather than an octahedral environment is associated with the influence of $d$ orbitals; the $ns^2-(n-1)d^{10}$ energy difference is about 5 eV for Hg, 10 eV for Cd and Zn.[7])

Regarding the cinnabar modification as the rocksalt-equivalent "ionic" form of the Hg compounds, we may interpret the cinnabar ↔ zinc-blende transition as an ionic ↔ covalent transition. All three materials lie close to this transition: The transition pressures (at low temperature) for HgSe and HgTe are very low, 7 and 14 kbar, respectively,[6] and the transition temperature (at low pressure) for HgS is 335°C.[5]

Phillips and Van Vechten (PVV) have recently reformulated Pauling's electronegativity concept in

[3] K. L. Aurivillius, Acta Chem. Scand. **4**, 1413 (1950).

[4] It is instructive to compare the Madelung energies of the two structures. We have calculated, using the Ewald method, the electrostatic binding energy for trigonal HgS: It is 1.04 times that of a rocksalt structure of equal density.

[5] O. L. Curtis, Jr., J. Appl. Phys. **33**, 2461 (1962).

[6] A. Jayaraman, W. Klement, Jr., and G. C. Kennedy, Phys. Rev. **130**, 2277 (1963); A. N. Mariano and E. P. Warekois, Science **142**, 672 (1963).

[7] L. E. Orgel, J. Chem. Soc. 4186 (1958); J. Phys. Chem. Solids **7**, 276 (1958).

TABLE I. Symmetry analysis and selection rules for the zone-center phonons in HgS.

| Representation | | Class characters 1 | $3_z$ | $2_x$ | Zone-center modes All $\Gamma$ | Acoust. $P$ | Opt. $\Gamma$-$P$ | Selection rules Infrared | Raman |
|---|---|---|---|---|---|---|---|---|---|
| Irred. reps. | $A_1$ | 1 | 1 | 1 | 2 | 0 | 2 | ··· | $\alpha_{zz}$, $\alpha_{xx}+\alpha_{yy}$ |
| | $A_2$ | 1 | 1 | −1 | 4 | 1 | 3 | $P_z$ | ··· |
| | $E$ | 2 | −1 | 0 | 6 | 1 | 5 | $P_x$, $P_y$ | $\alpha_{xy}$, $\alpha_{xz}$, $\alpha_{yz}$, $\alpha_{xx}-\alpha_{yy}$ |
| Unit-cell rep. | $\Gamma$ | 18 | 0 | −2 | | | | | |
| Vector rep. | $P$ | 3 | 0 | −1 | | | | | |

terms of a dielectric definition of ionicity.[8] Their fractional ionicity $f_i$ is given by $E_i^2/(E_h^2+E_i^2)$, where $E_h$ and $E_i$ are empirically obtained homopolar and ionic energy gaps. Applying the PVV prescriptions for $E_h$ and $E_i$ to HgS, we calculate $E_h=3.9$ eV and $E_i=6.7$ eV, yielding $f_i=0.75$, very close to their critical value of 0.78. The two characteristic energies place HgS squarely within the narrow ionic-covalent borderline area of $E_h-E_i$ space outlined by PVV. We obtain similar results for HgSe and HgTe. Thus the empirical PVV theory successfully "predicts" the borderline position of the Hg chalcogenides which is reflected experimentally in the observations of the preceding paragraph.

## 3. SYMMETRY AND SELECTION RULES

The HgS crystal of Fig. 1 belongs to space group $P3_121$ ($D_3^4$).[3,9] The six operations of the factor group are[10] 1, $3_1$, $3_1\times3_1$, 2, $3_1\times2$, and $2\times3_1$, where 1 denotes the identity; $3_1$ denotes a threefold rotation about the $c$ axis, followed by a $\frac{1}{3}c$ translation parallel to the axis; and 2 denotes a twofold rotation about an axis perpendicular to $c$. This symmetry is the same as that of quartz and the trigonal elemental semiconductors Se and Te, and the factor group has been discussed by several authors.[11,12] It is simply isomorphic to the familiar group $3m$ ($C_{3v}$) of the equilateral triangle and possesses three irreducible representations (I.R.'s), $A_1$, $A_2$, and $E$, where $A_1$ and $A_2$ are one-dimensional symmetric and antisymmetric (with respect to the twofold rotations) representations, and $E$ is a two-dimensional representation. The character table is contained in Table I.

The symmetries of the long-wavelength ($q\approx0$)[13] phonons are determined by $\Gamma$,[14,15] the factor-group representation generated by the displacements of the atoms in the unit cell. For HgS, $\Gamma$ is 18-dimensional and is, of course, reducible. The characters for $\Gamma$ are shown in the fourth row of Table I, and its reduction into I.R.'s is given in the fourth column: $\Gamma=2A_1+4A_2+6E$. Also listed in the table is the three-dimensional polar-vector representation $P$. The three zone-center acoustical phonons (rigid translations of the crystal) comprise such a representation, so that the I.R.'s of the optical phonons are contained in $\Gamma-P$: $2A_1+3A_2+5E$. There are thus ten optical-mode eigenfrequencies (ignoring for the moment the transverse-longitudinal splitting of the infrared-active modes), five nondegenerate $A$ modes ($2A_1+3A_2$), and five doubly degenerate $E$ modes.

Symmetry-determined selection rules governing the interaction of these vibrations with light are presented in the last two columns of Table I. For one-phonon optical absorption the mode induces a first-order electric moment $p$, so that it necessarily transforms as a vector. The infrared-active modes are therefore labelled by the I.R.'s common to $\Gamma$-$P$ and $P$; these are $A_2$ and $E$. The $A_2$ modes interact with light polarized parallel to the $c$ axis (= the $z$ axis of Table I), the $E$ modes with light polarized perpendicular to $c$. The symmetric $A_1$ vibrations do not interact with light in first order.

The two $A_1$ phonons, absent in the infrared spectrum, can be acquired in Raman scattering. A Raman-active vibration induces a first-order modulation in the di-

[8] J. C. Phillips and J. A. Van Vechten, Phys. Rev. Letters **22**, 705 (1969).

[9] This is for the right-handed form; for the enantiomorphic left-handed form, the space group is $P3_221$ ($D_3^6$).

[10] *International Tables for X-Ray Crystallography, Symmetry Groups* (Kynoch Press, Birmingham, England, 1952), Vol. 1, p. 257.

[11] R. H. Asendorf, J. Chem. Phys. **27**, 11 (1957); M. Hulin, Ann. Phys. (Paris) **8**, 647 (1963); A. Nussbaum, in *Solid State Physics*, edited by F. Seitz and D. Turnbull (Academic, New York, 1966), Vol. 18, p. 225.

[12] I. Chen and R. Zallen, Phys. Rev. **173**, 833 (1968).

[13] We specify $q\approx0$ rather than $q=0$ because of the complication, for infrared-active phonons, of photon-phonon interaction for $q$'s of the order of $\omega/c$. By $q\approx0$ we mean wave vectors small compared to the Brillouin-zone dimensions $q\ll\pi/a$, but large compared to the range of polariton effects $q\gg\omega/c$. The symmetries (I.R.'s) and degeneracies determined by the full crystal symmetry strictly apply only at $q=0$, where the infrared-active phonons are represented by the LO modes. We ignore the lowered symmetry away from $q=0$ and assume that the same I.R.'s and degeneracies apply, aside from TO-LO splittings, to $q\approx0$ phonons. Finite wave-vector asymmetry splittings of $E$ modes in quartz have been observed by A. S. Pine and G. Dresselhaus [Phys. Rev. (to be published)], and are extremely small ($\sim0.1$ cm$^{-1}$).

[14] A. S. Barker, Jr., Phys. Rev. **132**, 1474 (1963); **135**, A742 (1964); S. H. Chen, *ibid.* **163**, 532 (1967).

[15] R. Zallen, Phys. Rev. **173**, 824 (1968).

electric polarizability, so that it must transform as a component of a symmetric second-rank tensor. The selection rules for $D_3$ symmetry are given in the last column of Table I.[16] The $E$ modes, as well as the $A_1$, are permitted in Raman scattering. The presence of vibrations entitled to appear in both Raman and infrared spectra, the $E$ modes, is permitted by the absence of inversion symmetry. We return to this point in Sec. 9 in a discussion of pseudocentrosymmetric aspects of the observed spectra.

The analysis of Table I indicates that there are ten optical-phonon eigenfrequencies to be anticipated (ignoring the TO-LO splittings of the infrared-active modes, which increases the number to 18); eight of them ($3A_2+5E$) expected in reststrahlen, seven ($2A_1+5E$) in Raman scattering. Our experiments uncover nine (to be given in Table IV), one $E$ mode being missing.

## 4. EXPERIMENTAL TECHNIQUES

Far-infrared reflectivity was measured with a Perkin-Elmer 301 spectrometer, an instrument employing grating dispersion and an optical path purged with $N_2$ gas. The light source was a globar or a Hg arc, the detector a thermocouple or a Golay cell, depending upon spectral region. The spectrometer was operated single beam, reflected light intensity being measured in alternate scans of the sample and an Al mirror. Reflectivity was measured at an angle of incidence of 9°, and a wire grid was used to obtain polarized light. Phase detection at 13 cps was employed.

Raman scattering was excited with a 20-mW He-Ne gas laser and observed with a double-grating monochromator using photomultiplier detection, the output being presented in digital form through photon-counting circuitry. A coldfinger arrangement using a metal cryostat was employed for the measurement at liquid-nitrogen temperature. The He-Ne lasing photon energy of 1.96 eV is exceptionally fortunate for HgS, since it just slips under the fundamental absorption edge of the crystal.[2,17] The absorption coefficient crosses the 1-cm$^{-1}$ level at the beginning of the edge at 1.98 eV for $E\perp c$, 2.00 eV for $E\|c$. The proximity to the electronic interband threshold results in strong scattering intensities due to resonance enhancement.

Natural crystals of trigonal HgS were employed in this study. The best samples obtained, from the vicinity of San Luis Potosi, Mexico, were large isolated crystals embedded in limestone.[18] The single crystals used in the experiments were about 0.1 cm thick and 0.2 cm$^2$ in area. In addition, a large (>1 cm$^2$), polycrystalline sample from Idria, Yugoslavia, was used for some reflectivity measurements at the longest wavelengths where sensitivity is poorest. Analysis for impurities yielded concentrations below 0.01%. The optical quality of the crystals was quite good, residual absorption in the transparent region being less than 1 cm$^{-1}$.

After verifying that the reflectivity of carefully polished surfaces exhibited spectral structure as sharp as that of cleaved (but uneven) surfaces, detailed data were obtained on samples polished in several stages ending with a 0.05-$\mu$ particle-size alumina grit. The acceptability of polished surfaces for far-infrared reflectivity measurements, where the optical penetration depth is $\sim$10 $\mu$, is in contrast to the situation in the ultraviolet, where the penetration depth of $\sim$0.1 $\mu$ is comparable to the surface damage layer produced by polishing.

## 5. OBSERVED SPECTRA

In this section we display the experimental results. The reststrahlen spectra are shown in Fig. 3. The points

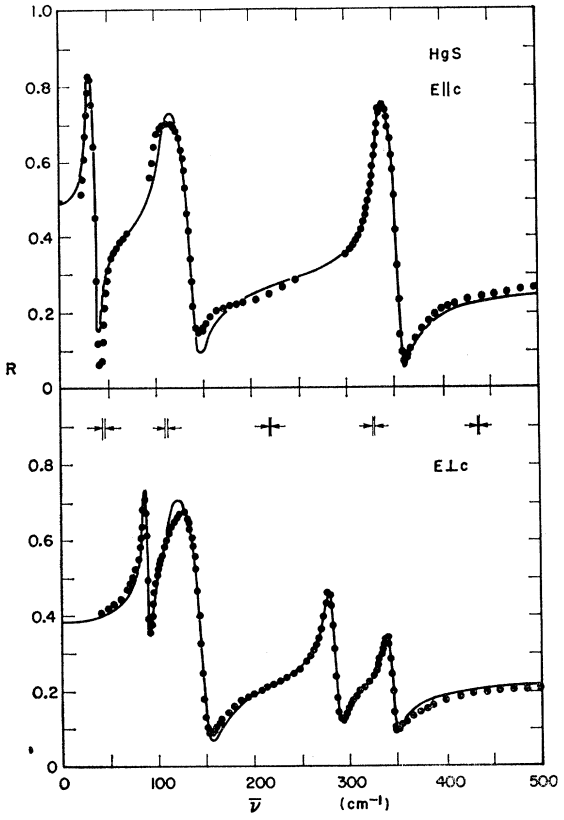


FIG. 3. Reststrahlen spectra of trigonal HgS. The points are the experimental results, the fitted curves correspond to the oscillator analysis. The experimental uncertainty in $R$ is about $\pm$0.04 over most of the range, somewhat more for $E\|c$ below 50 cm$^{-1}$. Points are omitted for $E\|c$ in two regions where the measured reflectivity was upset, by a few percent, due to a small admixture of $E\perp c$ structure introduced by low-angle twinning in the crystal.

[16] V. Heine, *Group Theory in Quantum Mechanics* (Pergamon, London, 1960), p. 452.

[17] The values quoted for $h\nu(\alpha=1\text{ cm}^{-1})$ apply to room temperature; at 80°K they have blue shifted by about 0.2 eV.

[18] Cinnabar samples were obtained from Ward's Natural Science Establishment, Rochester, N. Y., and Burnham Mineral Co., Monrovia, Calif.

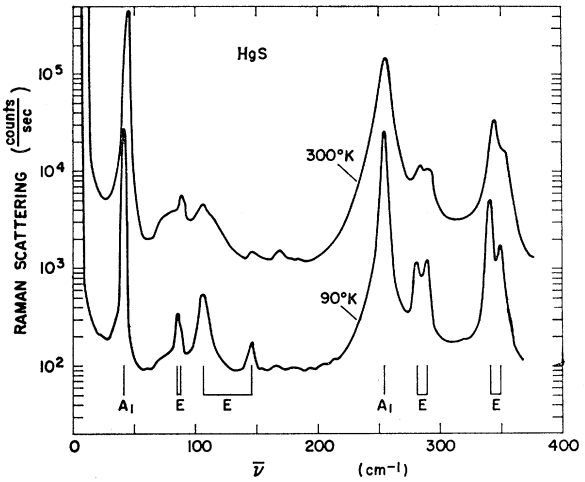


FIG. 4. Raman spectra of trigonal HgS. The room-temperature spectrum has been translated upward by one decade, for clarity. Spectral slit width is about 4 cm$^{-1}$.

represent the experimental data; the curves are theoretical fits discussed in Sec. 6. The data for $E\perp c$ were obtained with unpolarized light incident on a (0001) surface, a surface normal to the $c$ axis. The same spectrum, within experimental error, was observed using polarized light with $E\perp c$ incident on a $(10\bar{1}0)$ surface, a surface containing the $c$ axis and an $a$ axis. The data for $E\|c$ shown in Fig. 3 were determined with polarized light incident on a $(10\bar{1}0)$ surface, and is less accurate than that shown for $E\perp c$ due to the necessity for the polarizer. Below 50 cm$^{-1}$, the signal was too small to allow a reasonable direct measure of $R$ for $E\|c$, and in this region the points shown were obtained indirectly by combining results for $E\perp c$ with results obtained on a large polycrystalline sample in unpolarized light.

Three reststrahlen bands are observed for $E\|c$, four for $E\perp c$. The dielectric dispersion properties as well as the TO and LO frequencies deduced from these reflectivity results are discussed in following sections.

The Raman spectra at 300 and 90°K are presented in Fig. 4. Scattered light was observed at right angles to the incident beam, with the crystal's $c$ axis perpendicular to the plane of scattering. The spectra shown are Stokes spectra taken with circularly polarized incident light and no analyzer in the scattered beam. All of the Raman-active vibrations should be present for this geometry. The scattering is dominated by the two $A_1$ lines, the four TO-LO $E$ doublets are weaker by one or two orders of magnitude. Detailed discussion of the Raman results is deferred until Sec. 9.

## 6. DIELECTRIC DISPERSION PROPERTIES

In this section we deduce the optical properties from the experimental results of Fig. 3. Our procedure is to synthesize the observed reflectivity with a complex dielectric constant $\epsilon=\epsilon_1-i\epsilon_2$ constructed as a superposition of Lorentzians:

$$\epsilon(\bar{\nu})=\epsilon_\infty+\sum_j \frac{s_j\bar{\nu}_j^2}{-\bar{\nu}^2+\bar{\nu}_j^2+i\gamma_j\bar{\nu}_j\bar{\nu}}. \tag{6.1}$$

$\bar{\nu}_j, s_j$, and $\gamma_j$ are the oscillator frequency (in wavenumber units), oscillator strength (contribution to the static dielectric constant), and dimensionless damping constant, respectively, for oscillator $j$, and $\epsilon_\infty$ is the high-frequency dielectric constant. The final reflectivity fits are the curves of Fig. 3; the corresponding $\epsilon$'s are displayed on Fig. 5. The two $\epsilon$'s correspond to the two independent elements of the dielectric-function tensor for trigonal crystals: $\epsilon_{xx}=\epsilon_{yy}=\epsilon(E\perp c)$; $\epsilon_{zz}=\epsilon(E\|c)$. The oscillator parameters, which epitomize our experimental findings in the infrared, are contained in Table II.

The oscillator fits were arrived at by means of a computer program which performs an iterative search in parameter space. The optimization criterion was the minimization of the rms deviation of the fitted from the experimental reflectivity. For the final parameters of Table II, $\Delta R_{\rm rms}=0.019$ for $E\perp c$, 0.034 for $E\|c$. Initial parameters for beginning the search were chosen by examining the results of a Kramers-Kronig (KK) analysis of the data. The advantages of oscillator analysis over KK analysis have been well documented by A. S. Barker.[14]

The positions of the peaks in $\epsilon_2$ locate the frequencies of the $q\approx 0$ TO phonons. Also plotted in Fig. 5 is the energy-loss function $-\mathrm{Im}(\epsilon^{-1})$, which peaks at the LO phonon frequencies. (The zeros of $\epsilon_1$ cannot be used to determine the LO frequencies because of the finite damping. For example, the two weaker bands for $E\perp c$ have no $\epsilon_1=0$ intercepts whatever; damping prevents the weak oscillator strength from driving $\epsilon_1$ negative.) TO and LO frequencies are indicated by the bars on Fig. 5. The shaded regions between bars signify for-

TABLE II. Oscillator parameters fitted to $R(\bar{\nu})$.

| | $\bar{\nu}_t$ (cm$^{-1}$) | $s=\Delta\epsilon_1$ | $\gamma$ |
|---|---|---|---|
| | | $\epsilon_\infty=$ 9.9 | |
| $E\|c$ | 333 | 1.3 | 0.022 |
| | 110 | 7.1 | 0.11 |
| | 29 | 14.2 | 0.11 |
| | | $\epsilon_0=32.5$ | |
| | | $\epsilon_\infty=$ 8.25 | |
| $E\perp c$ | 338 | 0.27 | 0.031 |
| | 277 | 0.57 | 0.035 |
| | 111 | 6.5 | 0.14 |
| | 86 | 2.4 | 0.029 |
| | | $\epsilon_0=18.0$ | |

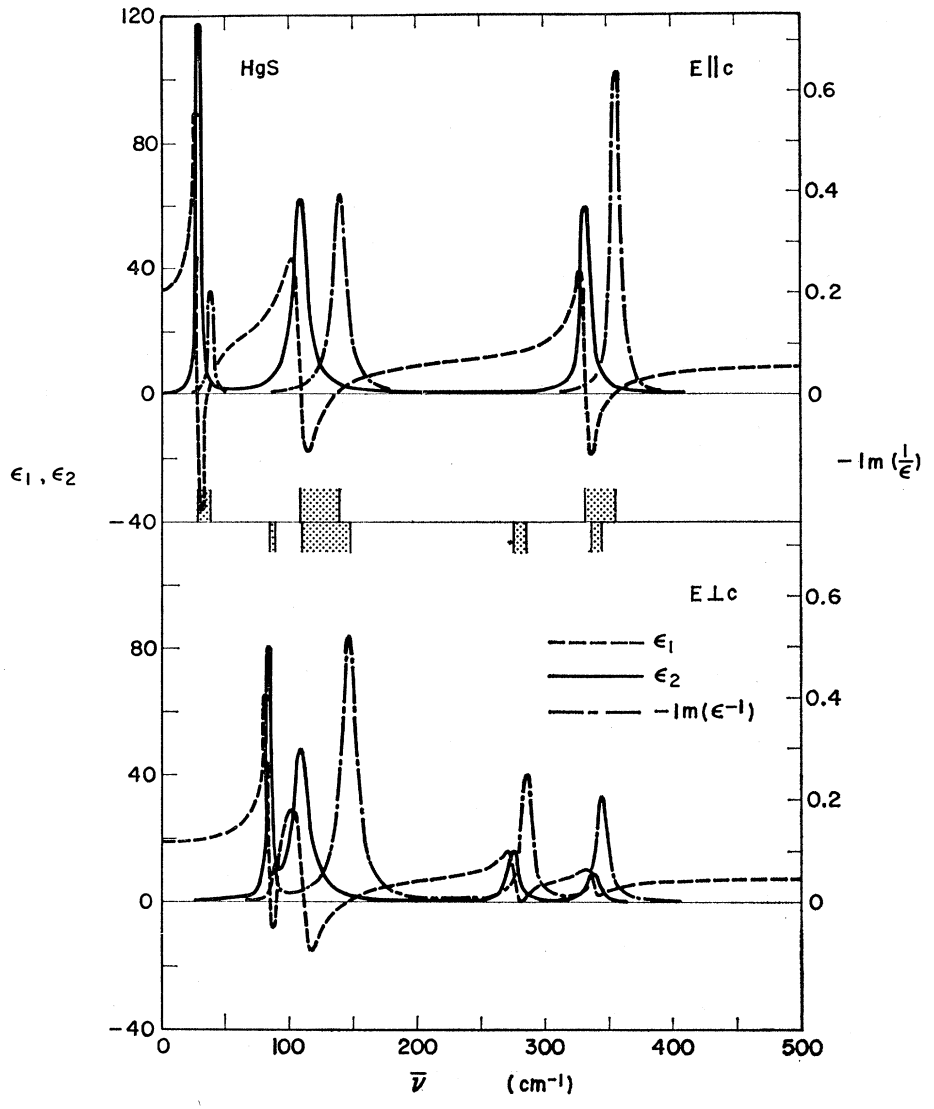


FIG. 5. Dielectric dispersion properties: $\epsilon_1$ and $\epsilon_2$ are the real and imaginary parts of the dielectric constant; $-\mathrm{Im}(\epsilon^{-1})$ is the energy-loss function.

bidden zones for long-wavelength phonons, frequency regimes in which there are no propagating waves. These are treated further in Sec. 7.

The complex refractive index $n^c=n-ik$ is computationally intermediate between $\epsilon$ and $R$: For $\epsilon \rightarrow n^c$,

$$n^2=\tfrac{1}{2}\epsilon_1+\tfrac{1}{2}(\epsilon_1^2+\epsilon_2^2)^{1/2}, \tag{6.2}$$

$$k^2=-\tfrac{1}{2}\epsilon_1+\tfrac{1}{2}(\epsilon_1^2+\epsilon_2^2)^{1/2}; \tag{6.3}$$

for $n^c \rightarrow R$,

$$R=[(n-1)^2+k^2][(n+1)^2+k^2]^{-1}. \tag{6.4}$$

Our results for $n$ and $k$ are shown in Fig. 6. At high frequencies our values for $n$ ($\epsilon_\infty^{1/2}$) are 10% higher than precise reported values[19] (at 1000 cm$^{-1}$) of 2.85 for $E\|c$ and 2.60 for $E\perp c$, indicating that our $R_\infty$'s are overestimated by 0.03–0.04. In the near-infrared transparent region, the index parallel to the optic axis exceeds the perpendicular index, $n(\|)>n(\perp)$, so that HgS is uniaxial positive, like $\alpha-SiO_2$, Se, and Te. [In the language of classical optics, $n(\|)$ is the extraordinary index, $n(\perp)$ the ordinary index.] The magnitude of $n(\|)$-$n(\perp)$ places HgS among the most highly birefringent crystals.

The oscillator strengths $s_i$ specify the increments in $\epsilon_1$ on passing through each reststrahlen band $\bar{\nu}_i$. Table II reveals that the lattice (infrared) contribution to the static dielectric constant $\epsilon_0$ is greater than the electronic (ultraviolet) contribution. The phonon contribution to $\epsilon_0$ is $\epsilon_0-\epsilon_\infty$, the interband contribution is $\epsilon_\infty-1$. For $E\|c$, $\epsilon_0-\epsilon_\infty=23$ and $\epsilon_\infty-1=9$; for $E\perp c$, $\epsilon_0-\epsilon_\infty=10$ and $\epsilon_\infty-1=7$. The anisotropy $(\epsilon(\|)-\epsilon(\perp))$ is larger for $\epsilon_0$ than for $\epsilon_\infty$, due primarily to the lowest-frequency resonance at 29 cm$^{-1}$.

[19] W. L. Bond, G. D. Boyd, and H. L. Carter, Jr., J. Appl. Phys. **38**, 4090 (1967).

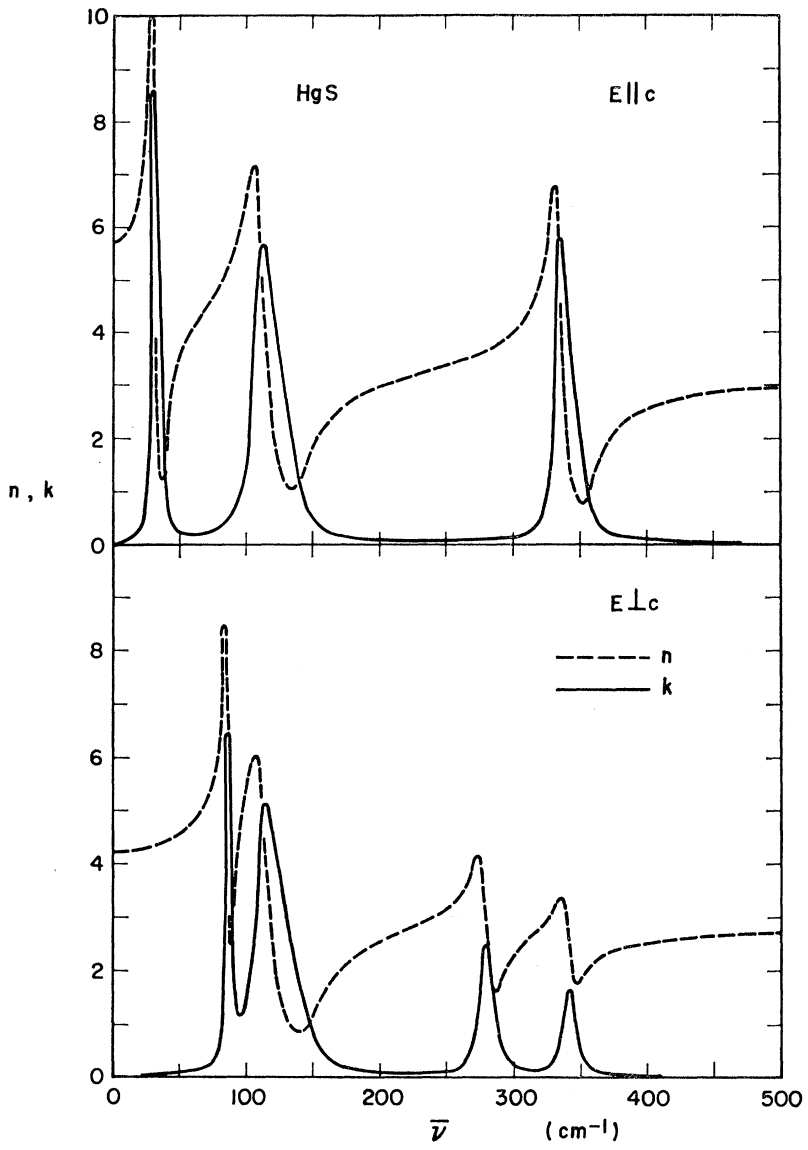


FIG. 6. The complex refractive index.

## 7. POLARITON DISPERSION CURVES

The strong photon-phonon interaction in the rest-strahlen region means that the correct elementary excitations of the system are coupled electromagnetic-lattice waves.[20] The results described in Sec. 6 enable us to determine dispersion curves for the polaritons (coupled photon-phonons). Using a complex propagation vector $q=q_1+iq_2$ to describe the coupled wave, then $q=(\omega/c)n^c$, so that the wave-number dependence of q is given by

$$q(\bar{\nu})=2\pi\bar{\nu}\cdot n^c(\bar{\nu}). \tag{7.1}$$

Using (7.1) and the $n^c$'s of Fig. 6 we obtain $q(\bar{\nu})$ and, thereby, $\bar{\nu}(q)$. The dispersion curves are presented in Figs. 7 and 8, for $E\perp c$ (with $q\|c$) and $E\|c$ (with $q\perp c$), respectively.

The solid curves in Figs. 7 and 8 are the experimentally defined polariton dispersion curves; they correspond to the fitted oscillator parameters of Table II. Letting the damping constants go to zero we obtain the dashed curves shown in the figures, which display the classical coupled-wave form. The $q=0$ intercepts of the zero-damping curves locate the LO frequencies; the $q\rightarrow\infty$ asymptotes determine the TO frequencies. For these curves, the regions in which $q$ is purely imaginary (bounded above and below by LO and TO frequencies, respectively) correspond to the stopping bands which were indicated by the shaded frequency regimes on Fig. 5.

[20] K. Huang, Proc. Roy. Soc. (London) **A208**, 352 (1951); J. J. Hopfield, Phys. Rev. **112**, 1555 (1968); E. Burstein, Comments Solid State Phys. **1**, 202 (1969).

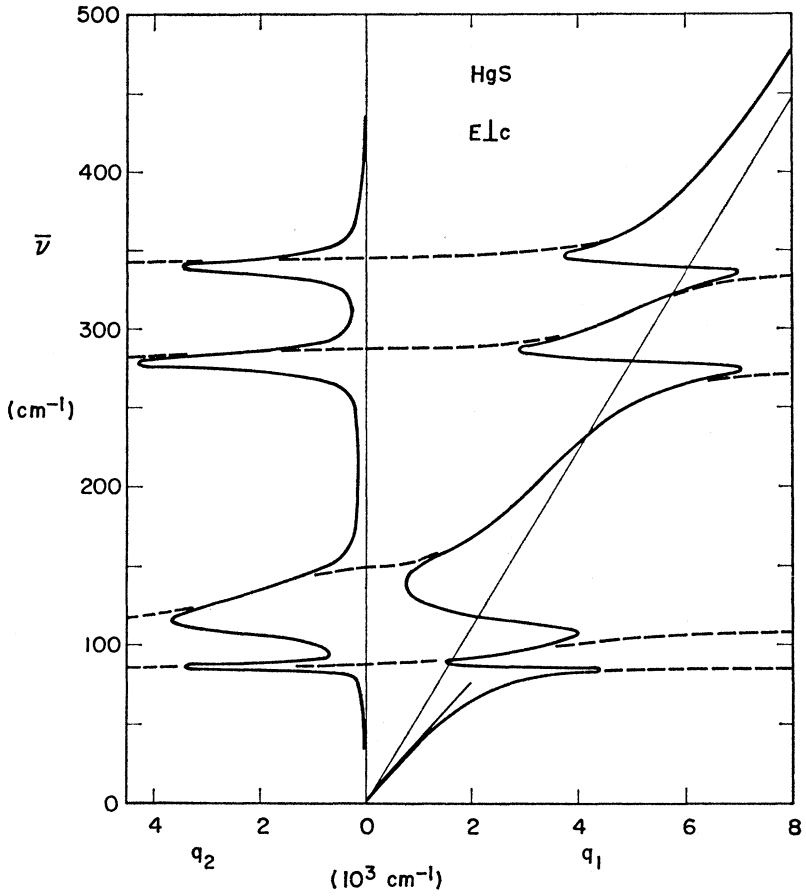


FIG. 7. Polariton dispersion curves for the $E$ modes.

The long and short straight lines shown on Figs. 7 and 8 have slopes of $(2\pi\epsilon_\infty^{1/2})^{-1}$ and $(2\pi\epsilon_0^{1/2})^{-1}$, inversely proportional to the optical and static refractive indices, respectively. The decrease in slope between high and low frequencies reflects the increase in $n$ on passing through the reststrahlen bands. With no photon-phonon interaction the dispersion curves would reduce to horizontal lines at the frequencies of the pure lattice waves, and to the long line representing the undisturbed light wave.

## 8. TO AND LO FREQUENCIES

At this juncture we take inventory of the $q\approx 0$ phonon frequencies and their symmetry assignments, as revealed by our experiments. The resulting catalog constitutes Table III. The experimental frequencies, derived as described below, appear in the last four columns of the table; the first three columns contain the mode symmetry, the polarization (transverse or longitudinal) of the infrared-active modes, and the composite estimate for $\bar{\nu}$.

The reststrahlen spectra of Fig. 3 have been subjected to the extensive dispersion analyses of Secs. 6 and 7, and the deduced frequencies are listed in the fourth and fifth columns of Table III. The symmetry assignments follow from the selection rules of Sec. 3. The TO frequencies are determined by the fitted oscillators of Table II; these are the positions of the $\epsilon_2$ maxima of Fig. 5 and of the $q\rightarrow\infty$ intercepts of Figs. 7 and 8. The LO frequencies are determined by the $q=0$ intercepts of the zero-damping curves of Figs. 7 and 8[21]; these are also the positions of the $-\mathrm{Im}(\epsilon^{-1})$ maxima of Fig. 5.

For the moment we treat the Raman spectra of Fig. 4 as line spectra, deferring a full discussion to Sec. 9. The peaks are sharp enough, especially at 90°K, to locate $\bar{\nu}_i$'s to within a few cm$^{-1}$. The lattice fundamentals expected in first-order scattering are the fully symmetric $A_1$ modes, Raman-active only, and the infrared-active $E$ modes. By far the strongest Raman lines are the two at 45 and 256 cm$^{-1}$, frequencies different from any seen in the infrared; these necessarily correspond to the $A_1$ vibrations. The remaining Raman lines, weaker by one or two orders of magnitude, can all be placed in TO-LO pairs corresponding to the four

[21] This is also equivalent to finding the zeros of the zero-damping $\epsilon_1(\bar{\nu})$.

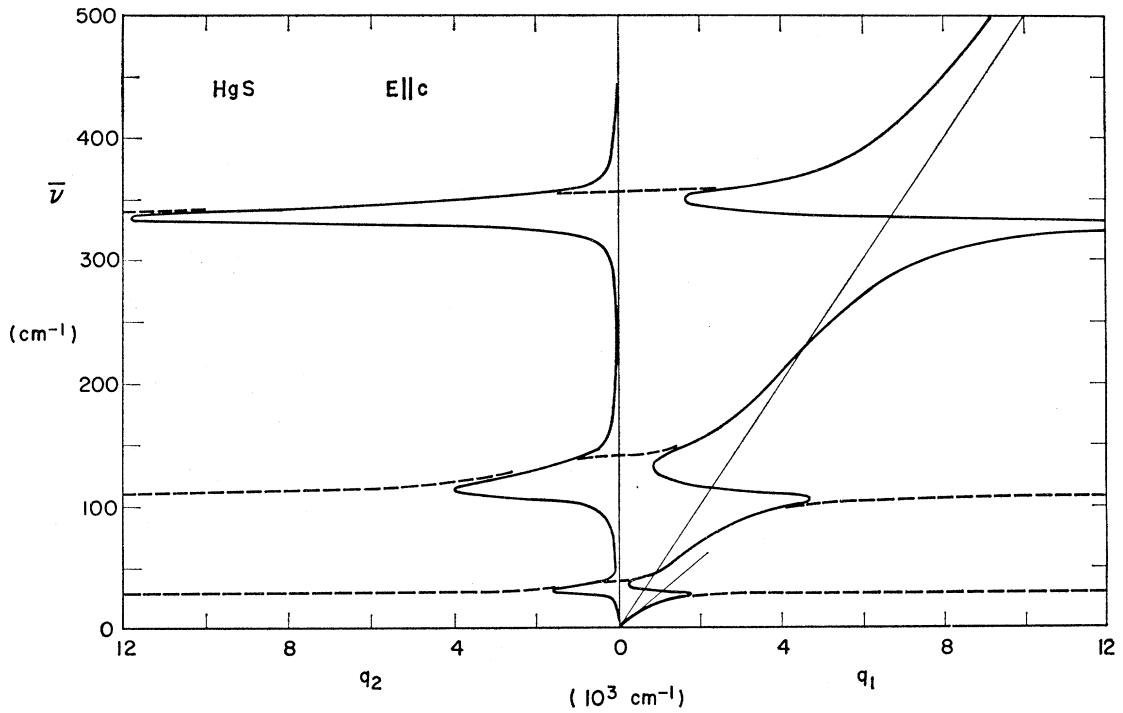


FIG. 8. Polariton dispersion curves for the $A_2$ modes.

$E$ modes observed in the $E\perp c$ reflectivity spectrum. The 87–91-cm$^{-1}$ pair is not quite resolved in Raman scattering.

## 9. RAMAN INTENSITIES

The scattering spectra of Fig. 4 were taken with the wave vectors of the incident and scattered photons perpendicular to each other and to $c$, so that the scattering vector lies in the $a$-$a$ plane. For propagation in this plane the $E$ vibrations are pure transverse or longitudinal. For right-angle scattering, the polariton wave vector lies well off to the right of the range contained in Fig. 7, so that the transverse $E$ modes occur very close to the TO frequencies, negligibly shifted by polariton effects. Polariton considerations do not enter, of course, for the longitudinal $E$ modes and the polarizationless $A_1$ modes; near $q\approx 0$, $\omega(q)$ is constant for these waves.

TABLE III. Long-wavelength optical-phonon frequencies ($\bar{\nu}$ in cm$^{-1}$) of HgS.

| Mode | $t$ or $l$ | $\bar{\nu}$ | Infrared $\bar{\nu}$ $E\|c$ | Infrared $\bar{\nu}$ $E\perp c$ | Raman $\bar{\nu}$ 300°K | Raman $\bar{\nu}$ 90°K |
|---|---|---|---|---|---|---|
| $A_2$ | $t$ | 29 | 29 | ··· | ··· | ··· |
| | $l$ | 39 | 39 | ··· | ··· | ··· |
| $A_1$ | ··· | 45 | ··· | ··· | 45 | 42 |
| $E$ | $t$ | 87 | ··· | 86 | 88 | 85 |
| | $l$ | 91 | ··· | 90 | 91 | 88 |
| $E$ | $t$ | 108 | ··· | 111 | 106 | 106 |
| $A_2$ | $t$ | 110 | 110 | ··· | ··· | ··· |
| | $l$ | 141 | 141 | ··· | ··· | ··· |
| | $l$ | 147 | ··· | 149 | 146 | 146 |
| $A_1$ | ··· | 256 | ··· | ··· | 256 | 254 |
| $E$ | $t$ | 280 | ··· | 277 | 283 | 282 |
| | $l$ | 288 | ··· | 287 | 290 | 289 |
| $A_2$ | $t$ | 333 | 333 | ··· | ··· | ··· |
| $E$ | $t$ | 342 | ··· | 338 | 345 | 341 |
| | $l$ | 350 | ··· | 346 | 353 | 349 |
| | $l$ | 357 | 357 | ··· | ··· | ··· |

With the incident beam circularly polarized and no analyzer in the scattered beam, the components of the polarizability-modulation tensor which contribute for this scattering configuration are $\alpha_{xy}$, $\alpha_{xz}$, $\alpha_{yz}$, and $\alpha_{zz}$. The $\alpha_{zz}$ component is generated by the $A_1$ modes, the others by the $E$ modes. To check that the two strongest lines in Fig. 4 are indeed the $A_1$ fundamentals, polarizers passing $E\|c$ were inserted in the incident and scattered beams to isolate $\alpha_{zz}$. This resulted in an order-of-magnitude reduction in the relative strength of the remaining ($E$) lines; it was not possible to achieve more complete polarization extinction with the samples studied.

The $A_1$, $E$(TO), and $E$(LO) frequencies obtained from the Raman spectra are listed in Table III. No appreciable frequency shift occurs between 90 and 300°K. The $E$ values are in quite reasonable agreement with the results deduced from the infrared dispersion analysis.

While our primary interest in the Raman emission is in the phonon frequencies derived, there are two interesting features of the observed intensities which we

discuss below: the relationship between Raman and infrared intensities, and the relative intensities of TO-LO doublets.

In crystals with inversion symmetry, there is mutual exclusion between infrared and Raman activity. While HgS lacks a center of symmetry and mutual exclusion does not hold, a striking feature of our data is the marked inverse correlation between Raman and infrared strength. While this complementarity is automatic for the $A_1$ and $A_2$ modes, it applies in more detail as well. The $\epsilon_0-\epsilon_\infty$ infrared contribution of the $A_2$ modes is more than twice that of the $E$ modes, which are also overshadowed in Raman scattering by the dominant $A_1$ lines. However, the Raman-infrared complementarity is most clearly demonstrated among the $E$ modes as, for example, the strongest and second-strongest $E$ Raman lines correspond to the weakest and second-weakest $E$ reststrahlen bands. If we list the normalized square roots of the observed $E$-mode intensities, we obtain a clear indication of the inverse correlation.

| $\tilde{\nu}$ | $I^{1/2}$(Ram) | $I^{1/2}$(inf) |
|---|---|---|
| 87 | 0.4 | 0.6 |
| 108 | 0.4 | 1.0 |
| 280 | 0.6 | 0.3 |
| 342 | 1.0 | 0.2 |

The complementarity noted above is reasonably associated with the rocksalt parentage of the cinnabar structure, i.e., the view of HgS as a geometric perturbation on a rocksalt structure. (The NaCl-HgS relationship is quite different than the Ge-GaAs relationship, which involves a chemical, or substitutional, perturbation.) Complementarity may then be regarded as a residual of the mutual exclusion exhibited by rocksalt. Note that for $\alpha$-quartz, which has the same crystal symmetry as HgS but which is not a perturbed-centrosymmetric structure, the statements of the preceding paragraph do not hold. Thus in quartz, $\epsilon_0-\epsilon_\infty$ is the same (to within 10%) for both $A_2$- and $E$-mode contributions,[22] while about half of the $E$ modes are simultaneously strong or weak in both Raman[23] and infrared, in contradiction of complementarity.

Besides the explicit dependence of the polarizability on the atomic displacements, $\Delta_Q\alpha=(\partial\alpha/\partial Q)Q$, the Raman scattering intensity for LO modes (with their attendant macroscopic field) also contains a contribution from the electro-optic effect, $\Delta_E\alpha=(\partial\alpha/\partial E)E$. For modes both infrared- and Raman-active, the relative intensities of the LO and TO Raman lines, $S(\mathrm{LO})/S(\mathrm{TO})$, provides information on the relative importance of electro-optic and atomic-displacement (or deformation potential) scattering mechanisms. This sort of analysis has been treated by several authors,[24,25] most recently and extensively by Ushioda.[26] Denoting the intensity ratio $S(\mathrm{LO})/S(\mathrm{TO})$ by $\rho$ and the polarizability-modulation ratio $\Delta_E\alpha/\Delta_Q\alpha$ by $\gamma$, the relation between the experimental and deduced ratios is approximately given by $\rho=|1-\gamma|^2$. From Fig. 4, $\rho\approx0.3$ for the HgS $E$ modes, yielding $\gamma\approx+0.5$; the atomic-displacement contribution is about twice the electro-optic.

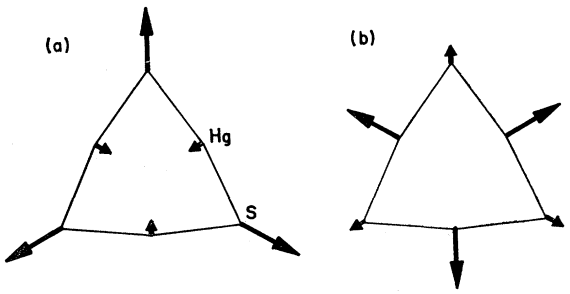


FIG. 9. Symmetrized coordinates for the $A_1$ vibrations, viewed along the $c$ axis: (a) corresponds to $\tilde{\nu}_+$, (b) to $\tilde{\nu}_-$.

Finally, we point out several subsidiary aspects of the scattering spectra of Fig. 4. The room-temperature spectrum exhibits a weak threshold at 65 $\mathrm{cm}^{-1}$ and a small peak at 167 $\mathrm{cm}^{-1}$. Both features, verified by observation in anti-Stokes scattering, are reduced in intensity at 90°K and are thus ascribable to second-order scattering.

## 10. VIBRATIONAL EIGENVECTORS

For Se and Te, the simplest helical-structure $D_3^4$-symmetry crystals, the $A_1$ and $A_2$ eigenvectors are determined by symmetry. For HgS, with twice as many unit-cell atoms, none of the optical-mode eigenvectors are symmetry determined; a specific model must be invoked for their calculation. In this section we present a rudimentary discussion of the eigenvectors of the nondegenerate $A$ modes. Atomic displacements in the two chain-breathing $A_1$ vibrations are derived from a very simple valence force model and the observed eigenfrequency ratio, while the $A_2$ (and, to a lesser extent, the $E$) vibrations are discussed in terms of rigid-ion and dynamic-charge contributions to the infrared intensities.

Figures 9 and 10 display orthogonal symmetrized displacements for the $A_1$ and $A_2$ optical modes. The actual eigenvectors may be any linear orthogonal combinations of Figs. 9(a) and 9(b) for the $A_1$ modes, and of Figs. 10(a), 10(b), and 10(c) for the $A_2$ modes. The particular symmetrized coordinates (SC's) shown were chosen to elucidate the discussion given below.

In the $A_1$ vibrations the atoms move along the twofold

[22] W. G. Spitzer and D. A. Kleinman, Phys. Rev. **121**, 1324 (1961).
[23] R. S. Krishnan, Nature **155**, 452 (1945).
[24] R. Loudon, Advan. Phys. **13**, 423 (1964).
[25] W. L. Faust and C. H. Henry, Phys. Rev. Letters **17**, 1265 (1966); S. Ushioda, A. Pinczuk, W. Taylor, and E. Burstein, in *II-VI Semiconducting Compounds*, edited by D. G. Thomas (Benjamin, New York, 1967), p. 1185.
[26] S. Ushioda, thesis, University of Pennsylvania, 1969 (unpublished); S. Ushioda, A. Pinczuk, E. Burstein, and D. L. Mills, in *Light Scattering Spectra of Solids*, edited by G. B. Wright (Springer, New York, 1969), p. 347.

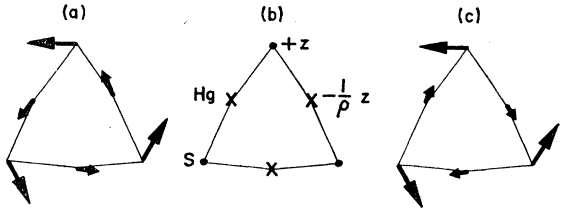


FIG. 10. Symmetrized coordinates for the $A_2$ vibrations, viewed along the $c$ axis.

axes, with one amplitude for the sulfurs and another for the mercuries. The simplest model for these vibrations includes only NN intrachain interactions. Let us assume bond-stretching and bond-bending forces which contribute terms to the potential energy of $\frac{1}{2}k(b-b_0)^2$ and $\frac{1}{2}k'b_0^2(\theta-\theta_0)^2$, respectively. Here $b$ and $b_0$ are the instantaneous and equilibrium bond lengths, $\theta$ and $\theta_0$ are the instantaneous and equilibrium bond angles, and $k$ and $k'$ are the bond-stretching and bond-bending force constants ($k'\ll k$). We include both Hg-S-Hg and S-Hg-S bond bending, assuming, for simplicity, equal force constants $k'$ for the two types of intrachain angle. Denoting the $A_1$ amplitudes by $u(\mathrm{S})$ and $u(\mathrm{Hg})$ and the corresponding atomic masses by $m$ and $\rho m$ (the mass ratio $\rho=m(\mathrm{Hg})/m(\mathrm{S})$ is 6.26), the assumed interactions along with the crystal geometry determine the following eigenvalue problem:

$$\begin{pmatrix} 0.736k+3.71k'-m\omega^2 & 0.080k-4.33k' \\ 0.080k-4.33k' & 0.009k+5.83k'-\rho m\omega^2 \end{pmatrix} \times \begin{pmatrix} u(\mathrm{S}) \\ u(\mathrm{Hg}) \end{pmatrix} = 0. \quad (10.1)$$

We now require that the ratio of the eigenvalues $\omega_+^2/\omega_-^2$ agree with the experimental value of $(256\ \mathrm{cm}^{-1}/45\ \mathrm{cm}^{-1})^2=32$. This determines $k'/k$ as 0.026 and, for the eigenvectors (which are schematically represented in Fig. 9),

$$\bar{\nu}_+=256\ \mathrm{cm}^{-1}, \quad u(\mathrm{Hg})/u(\mathrm{S})=-0.007; \quad (10.2)$$

$$\bar{\nu}_-=45\ \mathrm{cm}^{-1}, \quad u(\mathrm{S})/u(\mathrm{Hg})=+0.04. \quad (10.3)$$

These results indicate that the high- and low-frequency $A_1$ phonons correspond to nearly pure sulfur and mercury motions, respectively. [For (10.2), over 99% of the kinetic energy resides with the sulfurs; for (10.3) a like fraction resides with the mercuries.] This conclusion appears to be insensitive to details of the model; a similar result is obtained if, for example, we include only the bond-bending contribution of the Hg-S-Hg angles.

An examination of the coefficients of $k$ in (10.1) suggests that the disparity between $\bar{\nu}_+(A_1)$ and $\bar{\nu}_-(A_1)$ is due to the circumstance that $\bar{\nu}_-$ depends almost entirely upon bond bending for its restoring force. Since the two $A_1$ modes exhibit comparable Raman intensities although $\bar{\nu}_-$ involves very little NN bond stretching, the polarizability modulation cannot be simply accounted for on the basis of isotropic atomic polarizabilities dependent only on NN bond lengths.[27,28]

The SC's of Fig. 10 have been chosen for convenience in discussing the $A_2$ modes. Figure 10(a) displays a rigid rotation of the helical chain about the threefold axis. Since NN bond lengths and angles are preserved in this motion, it evidently corresponds to a true mode of zero frequency in the limit of noninteracting chains. The SC of Fig. 10(b) is a purely axial motion, with $z(\mathrm{S})/z(\mathrm{Hg})=-\rho=-6.26$ by orthogonality to the $z$ translation of the crystal (the $A_2$ acoustic mode). Figure 10(c) shows a counter rotation of the S and Hg helices, the amplitudes fixed by orthogonality to the chain-rotation SC of Fig. 10(a). We shall refer to the displacement of Fig. 10(b) as a rigid-sublattice SC since the S and Hg sublattices each undergo a rigid translation (i.e., all S-S and Hg-Hg spacings are preserved) during this motion. The rigid-sublattice SC corresponds to an optical-mode eigenvector in rocksalt.

A glance at Fig. 3 reveals that in the rigid-ion model,[29] in which each ion is assigned a point charge regarded to reside on and to move with the ion, only the rigid-sublattice SC would generate a first-order electric moment. Since all three $A_2$ fundamentals are observed in the infrared, the rigid-ion model would demand that the actual eigenvectors all contain a substantial admixture of the rigid-sublattice SC. However, the rigid-ion model fails to adequately account for infrared intensities even for the highly ionic alkali halides, in which $e^*/e$ differs substantially from 1. More dramatically, it predicts zero infrared intensity for all elemental crystals, yet Se and Te, *inter alia*,[15] exhibit strongly infrared-active fundamentals.[30] The mechanism for the electric moment in elemental crystals, and for the deviation from the rigid-ion expectation in ionic crystals, is the deformation or rearrangement of the electronic charge distribution induced by the atomic displacements during vibration. The effective charge associated with displacement-induced charge redistribution is referred to as dynamic charge.[12,31] Discussions

[27] Such a simple model has been successfully applied (Ref. 28) to the relative Raman intensities of the four $A_1$ modes of quartz. However these authors point out that an analogous simple model based on bond bending only yields results almost as good as those based on bond stretching only. Our results indicate that for HgS, polarizability-modulation contributions from bond bending and/or NNN bond stretching are comparable in importance to that from NN bond stretching.

[28] D. A. Kleinman and W. G. Spitzer, Phys. Rev. **125**, 16 (1962).

[29] M. Born and K. Huang, *Dynamical Theory of Crystal Lattices* (Oxford U. P., London, 1954).

[30] P. Grosse, M. Lutz, and W. Richter, Solid State Commun. **5**, 99 (1967); G. Lucovsky, R. C. Keezer, and E. Burstein, *ibid.* **5**, 439 (1967); R. Geick, U. Schroder, and J. Stuke, Phys. Status Solidi **24**, 99 (1967).

[31] E. Burstein, M. H. Brodsky, and G. Lucovsky, Intern. J. Quantum Chem. **1S**, 759 (1967); W. Cochran, Nature **191**, 60 (1961).

of the origin of dynamic charge in terms of bond deformation have been given by Kleinman and Spitzer[28] for $\alpha$-$SiO_2$ and by Chen and Zallen[12] for Se and Te. Dynamic charge allows infrared intensity to each of the $A_2$ modes in HgS even in the absence of an admixture of rigid-sublattice component.

In addition to the rigid-sublattice SC of Fig. 10(b), there are two others with the atomic motions along the $x$ and $y$ axes; these constitute a degenerate pair of SC's of $E$ symmetry. The three rigid-sublattice SC's are closely analogous to the optical-mode eigenvectors in rocksalt. It is natural to investigate the possibility that three vibrational eigenvectors of HgS consist predominantly of rigid-sublattice motions. We shall refer to this hypothetical $A_2+E$ triplet as the pseudocubic modes. Such modes would be expected to exhibit strong infrared intensity, very weak Raman intensity, low anisotropy, and the predominance of electrostatic over anisotropic interatomic forces. The first two of these criteria follow by analogy to NaCl, and the last two may be expressed by stating that the $A_2$-$E$ splitting be much smaller than the TO-LO splitting[24]:

$$|\bar{\nu}_t(A_2)-\bar{\nu}_t(E)| \text{ and } |\bar{\nu}_l(A_2)-\bar{\nu}_l(E)| \ll |\bar{\nu}_l(A_2)-\bar{\nu}_t(A_2)| \text{ and } |\bar{\nu}_l(E)-\bar{\nu}_t(E)|. \quad (10.4)$$

An examination of Tables III and IV (or of the forbidden frequency regimes shown shaded on Fig. 4) with respect to (10.4) reveals two $A_2$-$E$ frequency pairs as possibilities: at 108–110 $cm^{-1}$ and at 333–342 $cm^{-1}$. The 108–110-$cm^{-1}$ modes possess large, comparable TO-LO splittings, while the TO-LO splittings of the 333–342-$cm^{-1}$ modes are smaller and differ from each other by a factor of 3. Moreover, the 108-$cm^{-1}$ vibration exhibits the weakest Raman intensity among the observed $E$ modes, while the 342-$cm^{-1}$ mode gives rise to the strongest of the $E$ Raman lines. These considerations strongly favor the 108–110-$cm^{-1}$ eigenfrequencies as those appropriately assigned as pseudocubic vibrations, with eigenvectors possessing the largest admixture of rigid-sublattice displacements. In this frequency region the crystal behaves approximately isotropically, with a TO frequency at about 110 $cm^{-1}$ (108, 108, 110 for $E\|x,y,z$) and an LO frequency at about 145 $cm^{-1}$ (147, 147, 141 for $E\|x,y,z$).

## 11. EFFECTIVE CHARGES

Table IV summarizes much of our data and includes some additional information on the infrared strengths. The TO-LO splitting listed in the third column is the measure of infrared intensity which most clearly distinguishes the pseudocubic vibrations. (Zeros are entered for the $A_1$ phonons which are not polarization waves and which have no transverse or longitudinal character.) In column 4 we have tabulated the ionic plasma frequencies $\bar{\nu}_p$ defined by $\bar{\nu}_p^2=s\bar{\nu}_t^2/\epsilon_\infty$. In terms of the plasma frequencies, the zero-damping dielectric constant takes on the form

$$\epsilon(\bar{\nu})/\epsilon_\infty=1+\sum_i \bar{\nu}_{pi}^2/(\bar{\nu}_{ti}^2-\bar{\nu}^2). \quad (11.1)$$

This function can also be written directly in terms of transverse and longitudinal frequencies in a form which displays the $\bar{\nu}_t$'s as the poles and the $\bar{\nu}_l$'s as the zeros of $\epsilon$[32]:

$$\epsilon(\bar{\nu})/\epsilon_\infty=\prod_i (\bar{\nu}_{li}^2-\bar{\nu}^2)/(\bar{\nu}_{ti}^2-\bar{\nu}^2). \quad (11.2)$$

[Setting $\bar{\nu}=0$ in (11.2) yields the generalized Lyddane-Sachs-Teller relation for a complex reststrahlen spectrum.] For the case of a single reststrahlen band, the TO, LO, and ionic plasma frequencies are simply related by $\bar{\nu}_l^2=\bar{\nu}_t^2+\bar{\nu}_p^2$. With several bands present, the contributions to $\epsilon$ superimpose to shift the locations of the zeros; the LO frequencies are downshifted for the low-frequency bands and upshifted for the high-frequency bands. The quantity $\bar{\nu}_l-(\bar{\nu}_t^2+\bar{\nu}_p^2)^{1/2}$, which is a measure of this shift in $\bar{\nu}_l$ due to the presence of other polarization waves of the same symmetry, is given in column 5 of Table IV.

TABLE IV. TO-LO splittings and ionic plasma frequencies ($\bar{\nu}$ in $cm^{-1}$), and effective charges, of the zone-center modes.

| Mode | $\bar{\nu}_t$ | $\bar{\nu}_l-\bar{\nu}_t$ | $\bar{\nu}_p$ | $\bar{\nu}_l-(\bar{\nu}_t^2+\bar{\nu}_p^2)^{1/2}$ | $e^*/e$ |
|---|---|---|---|---|---|
| $A_2$ | 29 | 10 | 35 | −6 | ··· |
| $A_1$ | 45 | 0 | 0 | 0 | 0 |
| $E$ | 87 | 4 | 47 | −8 | ··· |
| $E$ | 108 | 39 | 96 | +3 | 0.41 |
| $A_2$ | 110 | 31 | 93 | −3 | 0.38 |
| $A_1$ | 256 | 0 | 0 | 0 | 0 |
| $E$ | 280 | 8 | 74 | −2 | ··· |
| $A_2$ | 333 | 24 | 121 | +3 | ··· |
| $E$ | 342 | 8 | 62 | +2 | ··· |

Effective charge is a tensor quantity governing the linear relation between the macroscopic polarization $\mathbf{p}$ and the atomic displacements $\mathbf{u}$: $\mathbf{p}=\mathbf{B}\mathbf{u}$.[15,33] For HgS, symmetry permits eight independent nonvanishing elements in the $3\times18$ rectangular matrix comprising $\mathbf{B}$. For a complex crystal, the problem of determining $\mathbf{B}$ from the experimental reststrahlen strengths requires a prior determination of the infrared-active vibrational eigenvectors. Although this information is largely lacking here, we shall invoke assumptions sufficient to allow an estimate of the two matrix elements corresponding to the pseudocubic vibrations discussed above.

For a cubic diatomic crystal, the total macroscopic polarization produced by the interionic displacement $\mathbf{u}=\mathbf{u}_+-\mathbf{u}_-$ is $[\frac{1}{3}(\epsilon_\infty+2)]\cdot ne^*\mathbf{u}$, where $n$ is the number of ion pairs per unit volume, $e^*\mathbf{u}$ is the unit-cell dipole moment set up directly by the atomic displacements (with $e^*/e$ an integer in the rigid-ion model), and $\frac{1}{3}(\epsilon_\infty+2)$ is the enhancement factor due to the addi-

[32] T. Kurosawa, J. Phys. Soc. Japan 16, 1298 (1961).
[33] M. Lax and E. Burstein, Phys. Rev. 97, 39 (1955).

tional action of the resultant local electric field on the electronic polarization.[29,34] The single parameter appearing in the effective charge tensor is then proportional to the ionic plasma frequency:

$$e^*=\pi^{1/2}cm^{1/2}\epsilon_\infty{}^{1/2}n^{-1/2}[3/(\epsilon_\infty+2)]\cdot\bar{\nu}_p, \quad (11.3)$$

where $m$ is the reduced mass $m_+m_-/(m_++m_-)$.

There is no simple generalization of (11.3) to apply to complex, anisotropic crystals. Not only does the reduced mass depend on the vibrational eigenvector, but, in the absence of the tetrahedral site symmetry needed for the derivation of (11.3), the local-field factor given by the term in square brackets must also be determined for each mode from the detailed crystal geometry. An example of a calculation of electrostatic forces in low-symmetry crystals is given in Ref. 12 for Se and Te. Lacking, at present, such a calculation for HgS, we proceed by naively applying (11.3) to the pseudocubic vibrations. We estimate $m$ by assuming the eigenvectors to be pure rigid-sublattice displacements. More drastic is the necessity, in the absence of better information, of using the cubic-symmetry local-field correction factor $3/(\epsilon_\infty+2)$. The results are listed in Table IV: $e^*/e\approx 0.4$ for these vibrations.

## 12. SUMMARY

An experimental investigation of the long-wavelength lattice vibrations of trigonal HgS has been carried out. The observed spectra of Figs. 3 and 4 have been analyzed to obtain the 16 zone-center optical-phonon frequencies listed in Table III. In addition to the standard dielectric dispersion properties, the infrared data have provided the polariton dispersion curves of Figs. 7 and 8 for the $E$ and $A_2$ modes. The Raman scattering is dominated by the $A_1$ lines, and the relative magnitudes of the TO and LO components of the $E$ doublets indicate that the atomic-displacement contribution to the polarizability modulation exceeds the electro-optic contribution. Marked complementarity between Raman and infrared intensity is noted and connected to a view of the HgS lattice as a geometric perturbation on the rocksalt structure. A simple NN valence-force model of the symmetric $A_1$ vibrations, taken together with the observed eigenfrequency ratio, indicates that the high- and low-frequency $A_1$ eigenvectors correspond to nearly pure sulfur and mercury motions, respectively. A discussion of the infrared-active modes suggests that the TO and LO modes at about 110 and 145 $cm^{-1}$ correspond to eigenvectors consisting largely of rigid-sublattice displacements such as shown in Fig. 10(b). With several assumptions, the effective charge of these pseudocubic vibrations is estimated.

## ACKNOWLEDGMENTS

The authors wish to express their appreciation to M. L. Slade for his able assistance with many experimental aspects of this work, and to A. T. Ward and Inan Chen for several valuable discussions.

[34] B. Szigeti, Trans. Faraday Soc. **45**, 155 (1949).